Physics of the Earth and Planetary Interiors 220 (2013) 37–49

Contents lists available at SciVerse ScienceDirect

Physics of the Earth and Planetary Interiors

journal homepage: www.elsevier.com/locate/pepi

Low strength of Earth's uppermost mantle inferred from tri-axial deformation experiments on dry olivine crystals

Sylvie Demouchy [a,*], Andréa Tommasi [a], Tiziana Boffa Ballaran [b], Patrick Cordier [c]

[a] Université de Montpellier 2 & CNRS, UMR 5342 Geosciences Montpellier, 34095 Montpellier, France
[b] University of Bayreuth, Bayerisches Geoinstitut, D-95440 Bayreuth, Germany
[c] Université Lille 1 & CNRS, UMR 8207 Unité Matériaux et Transformation, 59555 Villeneuve d'Ascq, France

ARTICLE INFO

Article history:
Received 5 February 2013
Received in revised form 15 April 2013
Accepted 17 April 2013
Available online 3 May 2013
Edited by George Helffrich

Keywords:
Olivine
Rheology
Upper mantle
Lithosphere
High-pressure experiment
TEM
EBSD

ABSTRACT

We have performed tri-axial compression experiments on single crystals of San Carlos olivine with various orientations at temperatures relevant for the uppermost mantle, between 800 and 1090 °C. The experiments were carried out at a confining pressure of 300 MPa in a high-resolution gas-medium mechanical testing apparatus at various constant strain rates (from $7 \times 10^{-6}\,s^{-1}$ to $1 \times 10^{-4}\,s^{-1}$); they yield differential stresses ranging from 88 to 754 MPa. Unpolarized infrared spectroscopy analyses indicate that hydrogen concentration in the olivine lattice is very low (<0.5 ppm wt H_2O) both before and after deformation. Transmission electron microscopy confirms plastic deformation by dislocation glide. [001] glide dominates regardless of the orientation of the crystals, even if very marginal [100] glide has also been activated in some samples. Orientation mapping by electron backscatter diffraction highlights significant local deviations from the original orientation in some samples associated with bending and deformation bands. These strain localizations suggest a heterogeneous mechanical behavior in this temperature range, which is favored by the strong mechanical anisotropy of the olivine crystal. The present experiments confirm that previous published high-temperature flow laws (i.e., power flow law) overestimate the strength of lithospheric mantle, since all samples deformed under stresses significantly lower than predicted by these flow laws. Based on the present results and on a compilation of previously published data on olivine deformation between 500 and 1000 °C, we propose a new semi-empirical exponential flow law applicable to the uppermost mantle:

$$\dot{\varepsilon} = 1 \pm 0.2 \times 10^{6} \exp\left\{-\frac{450 \pm 60 \times 10^{3}}{RT}\left[1 - \left(\frac{\sigma}{15 \pm 4}\right)^{1/2}\right]^{2}\right\}$$

where T is the absolute temperature, R is the gas constant, and σ is the differential stress in GPa. Subsequently, small fractions of melt or incorporation of hydrogen in olivine may not be required to reconcile natural observations indicating a limited strength of Earth's uppermost mantle lithosphere (<1 GPa) and experimental data on the rheology of olivine.

1. Introduction

Olivine is a key mineral for the Earth's upper mantle rheology, since it constitutes between 40% and 80% of its volume. The physical and chemical properties of olivine control the deformation and thermal exchanges in the mantle, the interactions between the lithosphere and asthenosphere, and the interactions with surface processes. Olivine is therefore one of the most studied rock-forming minerals and many experiments were performed to unravel its physical properties at high temperature (>1200 °C, e.g., Bai et al., 1991; Hirth and Kohlstedt, 1996; Mei and Kohlstedt, 2000a,b; Hirth and Kohlstedt, 2003; Faul et al., 2011). The plasticity of uppermost part of Earth's mantle, just below the Mohovičić discontinuity (Moho), which separates the crust and the mantle, is still poorly understood. Several questions are still debated. Does the mantle deform by brittle (elasto-plastic) or by ductile (viscous or viscoplastic) processes, such as dislocation or diffusion creep, in this layer? Or does it display an even more complex rheology with development of plastic instabilities, strain localization, and transient regimes?

Deformation experiments on olivine crystals and aggregates at low temperature are scarce. These data have often large

* Corresponding author.
E-mail address: demouchy@univ-montp2.fr (S. Demouchy).

0031-9201/$ - see front matter © 2013 Elsevier B.V. All rights reserved.
http://dx.doi.org/10.1016/j.pepi.2013.04.008

uncertainties (>30%) on the measured stresses (Phakey et al., 1972; Raleigh, 1968; Evans and Goetze, 1979; Gaboriaud et al., 1981) or were obtained at pressures much higher than those prevailing in the uppermost lithospheric mantle (i.e., >4 GPa; Raterron et al., 2004; Mei et al., 2010; Girard et al., 2010; Raterron et al., 2012). Detailed data on olivine plasticity at relatively modest temperatures (600–1000 °C), high stresses (>300 MPa) with satisfying high resolution on stresses (±10 MPa), and moderate pressure (<2 GPa), which are relevant for the uppermost mantle, are remarkably rare (Demouchy et al., 2009).

At high temperature, olivine deforms by an association of dislocation glide and diffusion-accommodated processes. Its rheological behavior is well described by power-law constitutive equations, which express the strain rate as a function of thermomechanical and microstructural parameters, including stress, pressure, temperature, silica activity, water and oxygen fugacity, and grain size. For single crystals of olivine, a complete set of constitutive equations already exists over a wide range of thermodynamic conditions based on one-atmosphere, compression deformation experiments or indentation data (Kohlstedt and Goetze, 1974; Durham and Goetze, 1977; Durham et al., 1985; Bai et al., 1991; Bai and Kohlstedt, 1992). These authors investigated the steady-state flow regime by deforming San Carlos olivine crystals with the compression axis parallel to the soft $[101]_c$, $[110]_c$, and $[011]_c$ directions, which favor glide on the dominant high temperature slip systems ([100](001) and [001](100) for $[101]_c$, [100](010) for $[110]_c$, and [001](010) for $[011]_c$). The notation with a subscript "c" indicates that the single crystal is compressed along a direction which is at 45° to two crystallographic axes and at 90° to the third axis (as in an equivalent fictive cubic lattice). However, at the lower and moderate temperatures and higher differential stresses relevant for the lithosphere, the olivine deformation mechanisms and resulting mechanical behavior are different (e.g., Raleigh, 1968; Phakey et al., 1972; Evans and Goetze, 1979; Demouchy et al., 2009).

The pioneering studies by Raleigh (1968) and Phakey et al. (1972) report results on single crystals of olivine deformed at temperatures ranging from 600 to 1250 °C using a solid-medium deformation apparatus (Griggs-type apparatus; Griggs, 1967). These constant strain rate tests exhibited work hardening even at 1000 °C, with differential stresses up to 1.2 GPa. Hardening was more marked at lower temperatures (600–800 °C). Olivines deformed in these experiments were characterized by optical microscopy and transmission electron microscopy (TEM; Phakey et al., 1972) allowing for the determination of active slip directions, but crystallographic orientation mapping techniques, like electron backscatter diffraction (EBSD), were unfortunately not available at these times.

Evans and Goetze (1979) employed micro-indentation experiments on olivine single crystals and polycrystalline samples at temperatures ranging from 21 to 780 °C to obtain the first low-temperature rheological laws for olivine. Based on these data, they proposed a transition from low-temperature, glide-controlled plasticity to high-temperature creep behavior at temperatures ranging from 900 to 1200 °C, depending on strain rate.

Innovative load relaxation experiments on polycrystalline samples of olivine were performed at pressures from 4.9–9.2 GPa using a DIA cubic anvil press coupled with X-ray diffraction and X-ray radiograph measurements within a synchrotron to estimate *in situ* differential stress and strain (Raterron et al., 2004). This study resulted in a flow law for olivine at low temperature (500–740 °C), which yields a mechanical behavior significantly weaker than predicted by the Evans and Goetze's (1979) law. These experiments have, however, significant uncertainties in stress and direct comparison to previous data is difficult due to the significant differences in confining pressure.

Demouchy et al. (2009) performed constant strain rate axial compression experiments at low temperature (900–1200 °C) on single crystals of olivine oriented in the $[101]_c$ direction using a gas-medium deformation apparatus (confining pressure of 300 MPa). These experiments also display yielding at lower stresses than predicted by the Evans and Goetze (1979) law, but the limited number of experiments and the single orientation did not allow defining a flow law.

Compression experiments using a deformation-DIA (D-DIA) coupled with X-ray, having alike problems with stress resolution, as Raterron et al. (2004), even after improvement, have also been performed on olivine +5% enstatite polycrystalline aggregates (Mei et al., 2010). The authors concluded, as did Demouchy et al. (2009), that stresses for olivine-rich rocks are weaker than expected from extrapolation of high temperature flow laws (e.g., Bai et al., 1991; Chopra and Paterson, 1984), but their flow law predicts significantly higher strengths than Raterron et al. (2004). The data sets on which these low temperature flow laws are based remain nevertheless restricted. Moreover, in all these studies, the determination of the flow law was simplified by fixing some parameters in the equations (i.e., the exponents p and q, see Kocks et al., 1975, p. 142). Similar assumptions in determining flow law equation were also adopted by Evans and Goetze (1979), Raterron et al. (2004) and Katayama and Karato (2008).

The present study aims to extend and refine the dataset on the deformation of olivine at lower temperatures and higher differential stresses by deforming single crystals under various crystallographic orientations in a gas-medium deformation apparatus, which allows a high-resolution stress measurement. The resulting microstructures were fully characterizing by EBSD mapping and TEM analyses in order to characterize the active deformation processes. These experiments aim to further constrain the deformation processes and the strength of the Earth's uppermost mantle.

2. Experimental and analytical methods

2.1. Sample preparation

Sizeable gem-quality of olivine single crystals from San Carlos (Arizona) were selected for the deformation experiments. They were crystallographically oriented using of two single-crystal X-ray diffractometers at the Bayerisches Geoinstitut (University of Bayreuth, Germany). First, intensity data were collected using a kappa-geometry Xcalibur™ diffractometer with Mo Kα radiation, equipped with a charge-coupled device (CCD) camera and a graphite monochromator. The Xcalibur™ diffractometer operates at 40 kV and 30 mA. Several frames were collected using omega scans and an exposure time of 1s in order to assess the quality of the crystals. The crystals for which all reflections of the collected frames could be indexed uniquely with a single orientation matrix were then moved onto a Huber single-crystal four-circles diffractometer, operating at 50 kV and 40 mA with Mo Kα radiation. The orientation matrices determined from the Xcalibur measurements were used to orient the crystals along one of the main crystallographic axes [100], [010] or [001]. The diffraction peaks of the most intense reflections among the three crystallographic directions of each olivine crystal (typically [200], [020], or [004]) were carefully centered. Centering of the chosen reflections was sometimes difficult due to the broad diffraction peaks. This resulted in an angle mismatch between the ideal crystallographic axis and the one actually oriented of ±1–7°. After orientation, the tip of the crystal was dipped into a thick drop of UV-curing epoxy (type Loctite™ 350), laid down on a horizontal glass slide (horizontality was ensured by a bubble inclinometer), and fixed with 5 UV pulses of 20 s each (for further details see Jacobson et al., 2005).

Once one crystallographic direction was known, the two others were defined using optical microscopy and polarized-analyzed light. Cylinders with a diameter of 2.8 mm or 4.2 and between 4 and 8.01 mm in length were drill-cored with the long axis subparallel to a $[1\,0\,1]_c$, $[0\,1\,1]_c$, or $[1\,1\,0]_c$ direction or at an odd crystallographic orientation; the present experimental specimens are therefore larger than in Demouchy et al. (2009). Only olivine cylinders free of cracks, lily pads (Mosenfelder et al., 2006), or inclusions were selected for deformation. San Carlos olivines have typical mantle-derived composition with $(Mg_{0.91}Fe_{0.09}Ni_{0.003})_2SiO_4$. The water content of San Carlos olivine is naturally very low (less than 5 ppm wt H_2O). Nevertheless the olivine cylinders were dried out using a 1-atm creep apparatus at 1250 °C for 24 h in a Ni crucible and under a flux of $Ar_{99\%}H_{1\%}$ gas-mixture (1% of H is added to avoid oxidation).

For experiments at $T \geqslant 1000$ °C, the samples were placed into thick-walled cylindrical sleeves of nickel (Ni) with an outer diameter of 9.90 mm and heights equal to those of the olivine cylinders (Fig. 1). For experiments at $T < 950$ °C, silver (Ag), which has a melting temperature of 961 °C at room pressure, was used as a sleeve material. At these low temperatures, the Ag sleeve supports a negligible portion of the load (equivalent to ~2 MPa at 800 °C, see Frost and Ashby, 1982 and Demouchy et al., 2009). To buffer oxygen fugacity and silica activity, each cylinder of olivine was coated with an aqueous mixture of Ni–NiO and fined-powdered enstatite, then dried under vacuum at 60 °C for 3 h, and fitted into its Ni or Ag sleeve. A 20 μm thick disc of nickel was placed at either end of each olivine cylinder.

Deformed olivine samples were recovered by dissolving the iron jacket and Ni sleeve using *aqua regia* (i.e., chloric acid plus nitric acid with a volume ratio of 1:1). The Ag sleeves were dissolved in nitric acid at 60 °C for 3 h under a fume hood. A few samples could not be recovered in a single piece after the dissolution of the jacket or sleeve due to the exothermic reaction and/or quench-related fractures. Nevertheless, enough samples were successfully recovered (Fig. 1c) and subsequently prepared for Fourier transform infrared spectroscopy (FTIR), EBSD, and TEM.

2.2. Deformation experiments

Tri-axial compressive deformation experiments at constant displacement rates were performed at $800 \leqslant T \leqslant 1090$ °C on oriented olivine crystals using a high-resolution gas-medium high-pressure apparatus with an uncertainty in differential stress less than 20 MPa. The confining pressure was 300 ± 2 MPa. Temperature was increased at a rate of ~10 °C/min before the application of the load and decreased at a rate of 100 °C/min at the end of an experiment by slowly decreasing power (*N.B.*, abrupt power shut down generally induces severe damage of the high-temperature furnace). Temperature gradients are less than 2 °C along the length of the sample and temperature was rigorously kept stable during the mechanical experiment since a small variation in temperature could yield to important load variation. To determine the contribution of the iron jacket and of the metal sleeve to the measured load, flow laws for Fe, Ni, and Ag from Frost and Ashby (1982) were used. Values of stresses and strain rates were corrected for instantaneous changes in cross-sectional area of the metal jacket, sleeve, and olivine cylinder during deformation assuming that samples maintained a cylindrical shape. These corrections of mechanical data are identical to corrections used in several published experimental studies on olivine deformation in a gas-medium deformation apparatus (e.g., Karato et al., 1986; Mei and Kohlstedt, 2000a,b; Chen et al., 2006; Demouchy et al., 2009), ensuring that this source of uncertainty was properly assessed.

2.3. Fourier transform infrared analysis

The water content, or more precisely, the concentration of hydrogen as atomic impurities in the olivine crystals, was checked after annealing at 1-atm and prior to deformation experiments. Hydrogen was detected within the samples with a FTIR Bruker IFS66V/S spectrometer coupled with an Bruker HYPERION-IR microscope, with unpolarized mid-infrared radiation (Globar source) and a MCT detector at the Laboratoire des Colloïdes, Verres et Nanomatériaux (LCVN) at Université Montpellier 2 (France). A

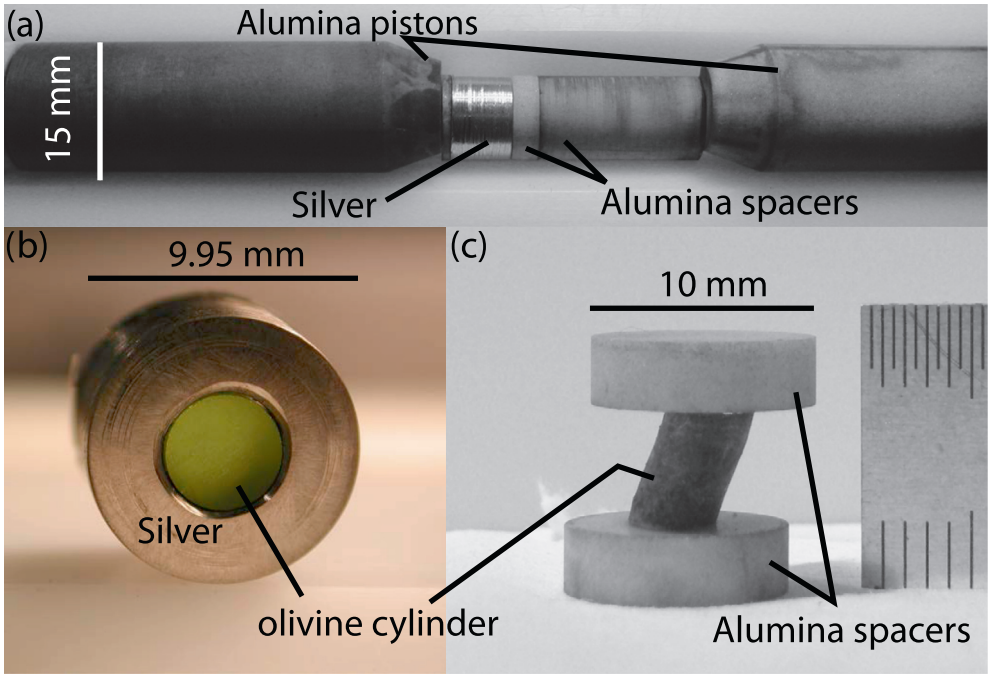

Fig. 1. Pictures of (a) the high pressure assembly without the iron jacket (run PoEM 5), (b) a silver plug with a single crystal of olivine inside (PoEM 5), and (c) a post-deformation olivine crystal (PoEM 11).

slice of an untreated San Carlos olivine crystal (3.066 mm thick), a piece of dried out olivine crystal (1.863 mm thick) and a section of a deformed sample (PoEM 7, 1.45 mm thick), which was cut perpendicular to the compression axis, were carefully double-polished by hand using diamond lapping-films (with grid from 30 to 0.5 μm). A squared aperture of 100 μm was used and 200 scans were accumulated per spectrum at a resolution of 4 cm^{-1}. The measurements were done at the center of the each olivine slab. For each FTIR spectrum, and after background subtraction, baseline rectification, and thickness normalization to 1 cm, the hydroxyl content was quantified using the calibration of Paterson (1982) as detailed in Demouchy (2010). We used a density factor of 2695 wt ppm H_2O for olivine Fo_{90} (e.g., calculation method given by Bolfan-Casanova et al., 2000). This calibration may underestimate the water content for olivine (Libowitzky and Rossman, 1997; Bell et al., 2003; Withers et al., 2012), however the aim of the present study is not to quantify the absolute hydrogen concentration, but only to confirm the absence of hydrogen in the olivine starting material before and after deformation. Finally, Ti as atomic impurities might be responsible for H incorporation in olivine as suggested by Berry et al. (2007), but since the H concentration is very low, Ti is likely to play a negligible role here.

2.4. Electron backscattered diffraction

We analyzed the microstructure of several deformed crystals by orientation mapping by EBSD. This approach enables quantifying the lattice distortions and misorientations within the deformed crystals, and hence, identifying any potential strain heterogeneity. To ensure high-quality scanning electron microscopy (SEM) imaging and EBSD analyses, polishing with diamond paste was followed by polishing with colloidal silica suspension to remove the mechanical damage at the specimen surface. EBSD analyses were conducted with a CamScan X500FE CrystalProbe equipped with an EBSD system at Geosciences Montpellier (France). The operating conditions were a current of 15 kV and 2.5–3.9 nA and a working distance of 20 mm. Low vacuum conditions (4–5 Pa of gaseous nitrogen) were used to avoid electron charging of the samples, in particular at the edges. The geometry of the CrystalProbe-EBSD is detailed in Demouchy et al. (2012). Data were acquired and treated with the HKL CHANNEL5 software by Oxford Instruments.

Several crystal orientation maps were acquired with a sampling step size of 20 μm (PoEM 11, 19), 25 μm (PoEM 9, 11, 15), or 50 μm (PoEM 8, 18, 19). These maps cover up a minimum of half of the longitudinal section (i.e., the section containing the compression axis) of each sample. The mapped areas ranged between 1425 × 1150 μm and 6500 × 5600 μm. Raw indexation rates were >85%. Data treatment allowed the rare non-indexed pixels to be filled if up to six identical neighbors existed with this orientation. EBSD maps were colored as a function of the orientation at one end of the sample and misorientation profiles were quantified using the processed maps. A minimum of 3000 points was analyzed in each map, ensuring a good statistical analysis of the misorientation within the crystal. Pole figures and inverse pole figures were constructed to display the initial and final sample orientation and the rotation of the main crystallographic axes [100], [010], and [001] relative to the initial coordinates.

2.5. Transmission electron microscopy

TEM has been used to characterize the microstructures after deformation of six selected samples: PoEM 8, 9, 11, 15, 18, and 19. Doubly polished thin sections (30–25 μm thick), parallel or perpendicular to the compression axis, have been prepared from the recovered specimens for TEM observation. These sections have been glued on a Mo grid and ion milled at 5 kV under a low beam angle of 15° until electron transparency was reached. TEM observations were carried out in Lille (France) using a Philips CM30 microscope operating at 300 kV and a FEI Tecnai G20 microscope operating at 200 kV. Sample orientation was achieved by using selected-area electron-diffraction and precession electron diffraction with a "Spinning Star" precession module from the Nanomegas Company. Simulated kinematical diffraction patterns were calculated using the "Electron Diffraction" software (Morniroli and Steeds, 1982).

3. Results

3.1. Hydrogen concentration

FTIR measurements were performed to check if the starting material was dry. Unpolarized infrared spectra are shown in Fig. 2. Infrared spectra demonstrate that a very low hydrogen concentration of 14–20 $H/10^6$ Si, (equal to 1–2 ppm H_2O by weight for Fo90) was present in the untreated large gem olivine crystals from San Carlos selected for the experiments. Both the heat-treated and the deformed olivine crystals were found to be dry. Thus annealing at high temperature was efficient to fully dry out the hydrogenated point defects in olivine.

3.2. Mechanical data

Experiments were conducted at constant displacement rates ranging from 7.06×10^{-6} to 1.0×10^{-4} s^{-1} at temperatures between 800 and 1090 °C and confining pressures of 300 MPa to produce tri-axial finite strains ranging from ~1% to 23%. Experimental conditions and mechanical data for the 16 runs are provided in Table 1. Samples recovered after the experiments showed few fractures, which are likely to be linked to the final mechanical failure at the very end of the deformation experiment. A clear shear band in the external soft metal sleeve confirms this final rupture (often visible after partial dissolution by *aqua regia*).

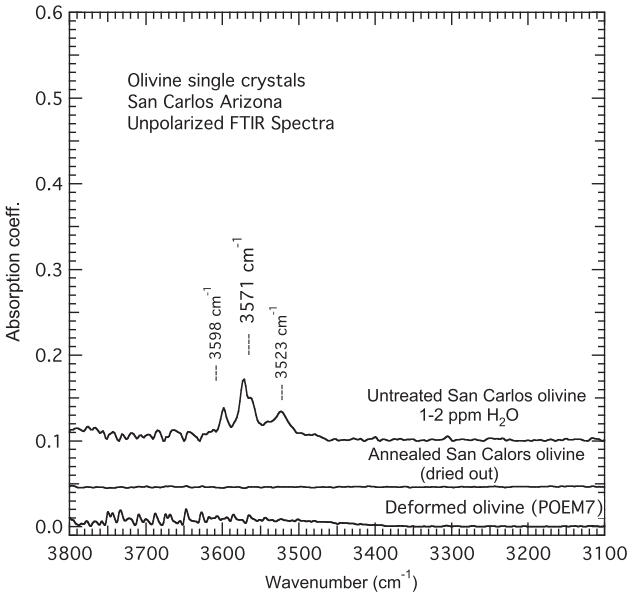

Fig. 2. Unpolarized FTIR spectra for the San Carlos olivine specimens. Starting material contains limited amount of hydrogen and has characteristic IR bands for natural mantle-derived olivine (top spectrum). Annealed olivine cylinder prior to deformation (center spectrum), and deformed olivine samples (bottom spectrum) are both dry. All spectra are normalized to 1 cm of thickness.

Table 1
Deformation experiments types, experimental conditions and mechanical data.

	[uvw] group	[uvw]* Tabulated	Initial L (mm)	Initial D (mm)	Metal sleeve	Expt. type	Temp. (°C)	Strain rate (s^{-1})	Max diff stress (MPa)	Total strain (%)	Diff. stress for strain 1%
POEM 5	[u0w]		6.08	2.86	Ag	Const. Disp	850	1.01×10^{-5}	503	10.4	201
POEM 6	[u0w]		7.19	2.86	Ag	Const. Disp	880	1.04×10^{-5}	708	22.2	307
POEM 7	[u0w]		5.93	2.86	Ag	Const. Disp	875	1.09×10^{-4}	713	17.5	577
POEM 8	[u0w]	[10 4 19]	7.04	4.15	Ni	Const. Disp	1090	1.07×10^{-5}	498	7.4	130
POEM 9	[u0w]	[101]	6.32	4.19	Ag	Const. Disp	806	5.1×10^{-5}	754	10.1	719
								1.2×10^{-5}	707	1.1	700
POEM 10	[0vw]		5.12	4.20	Ag	Const. Disp	800	1.01×10^{-5}	412	22.2	132
POEM 11	[0vw]	[5 19 10]	6.61	4.20	Ag	Const. Disp	850	7.06×10^{-6}	454	21.5	113
POEM 12	[0vw]		6.56	4.20	Ag	Const. Disp	900	1.02×10^{-5}	670	23.3	43
POEM 13	[0vw]		8.02	4.20	Ag	Const. Disp	945	8.3×10^{-6}	600	9.1	22
POEM 14	[0vw]		7.97	4.20	Ag	Const. Disp	850	1.01×10^{-5}	150[a]	10.0	60
POEM 15	[0vw]	[011]	5.46	4.20	Ag	Const. Disp	850	1.04×10^{-5}	473[a]	4.7	75
POEM 16	[uv0]		4.12	4.20	Ag	Const. Disp	800	7.08×10^{-6}	119	12	54
								2.01×10^{-5}	171	4.2	70
POEM 17	[uv0]		5.45	4.20	Ag	Const. Disp	800	1.01×10^{-5}	430	5.4	53
POEM 18	[uv0]	[121]	5.24	4.20	Ag	Const. Disp	900	8.11×10^{-6}	125	6.8	16
POEM 19	[uv0]		5.29	4.20	Ag	Const. Disp	900	1.01×10^{-5}	466	18.8	30
POEM 20	[uv0]	[5 19 10]	5.48	4.20	Ag	Const. Disp	850	9.88×10^{-6}	276	7.1	43

Abbreviation: Const. Disp., constant displacement rate experiment.
[a] Single crystal broke during experiment.
* Tabulated [uvw] orientations of the compression axis from EBSD measurements. Cell parameters of olivine (Fo_{96}) from Deer et al. (1997, p. 7). POEM 5–9 close to [101]c, POEM 10–16 close to [011]c, and POEM 11–19 close to [110]c.

The olivine crystals were deformed with the compressive axis initially parallel to directions of the type [u0w], [0vw], or [uv0] as well as in odd directions (sample 18 where the compression is applied close to $[111]_c$ direction). Therefore, in the subsequent section, we present the mechanical results as a function of the sample orientation: [u0w], [0vw], or [uv0] and odd as group 1, 2, and 3, respectively. Note that our olivine samples were not perfectly oriented parallel to the soft $[101]_c$, $[110]_c$, and $[011]_c$ directions; which may result in overestimation of the stresses.

3.3. Orientations [u0w]

Tri-axial compression parallel to directions [u0w], that is between [100] and [001], permits simultaneous activation of two to four slip systems: [001](100) and [100](001), as well as [001](110) and [100](011). The mechanical responses of olivine crystals in this group at various temperatures and at constant displacement rates are illustrated in Fig. 3. Except for PoEM 5 and PoEM 8, which have been deformed at higher strain rates ($>10^{-5}\ s^{-1}$), all experiments exhibit consistent behaviors. Plastic yield is followed by a parabolic "hardening" regime until a plateau is reached. At similar strain rates, differential stresses increase with decreasing temperature and a maximum stress of 719 MPa is obtained at 800 °C for a strain rate of $5.1 \times 10^{-5}\ s^{-1}$. The initial work-hardening stage is more marked in the highest temperature experiment (PoEM 8 at 1090 °C). This run having been terminated at rather low strain, it is difficult to infer whether this hardening stage would have been followed by a steady-state regime. One experiment at 850 °C (PoEM 5) shows a distinct behavior. Initial cracking while starting the deformation experiment (i.e., when

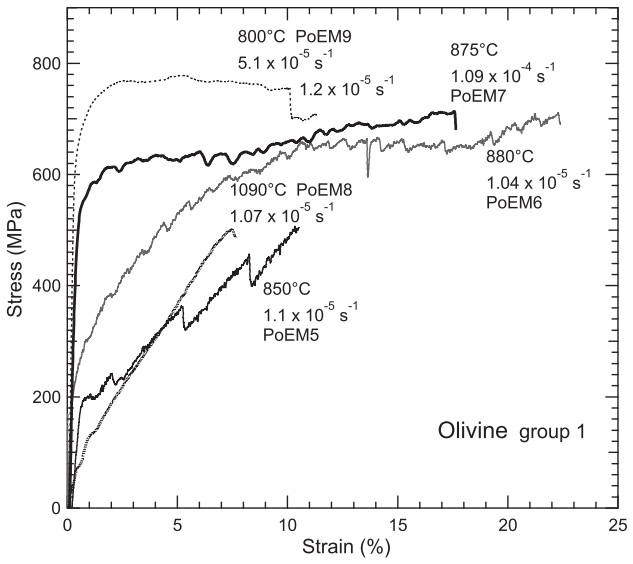

Fig. 3. Stress versus strain for constant displacement rate experiments for deformed olivine single crystals (group 1).

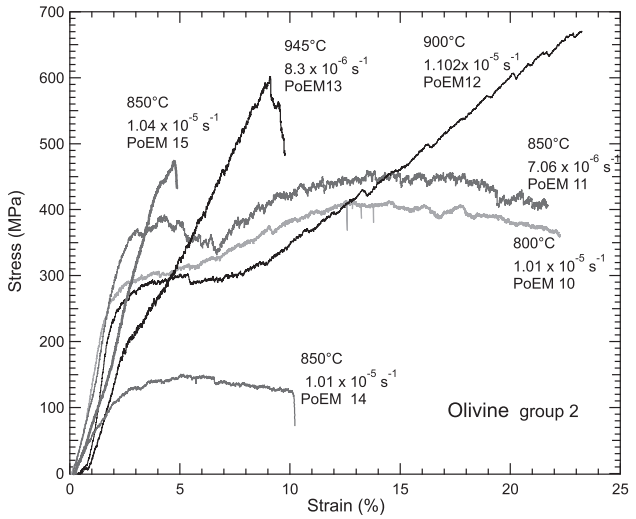

Fig. 4. Stress versus strain for constant displacement rate experiments for deformed olivine single crystals (group 2).

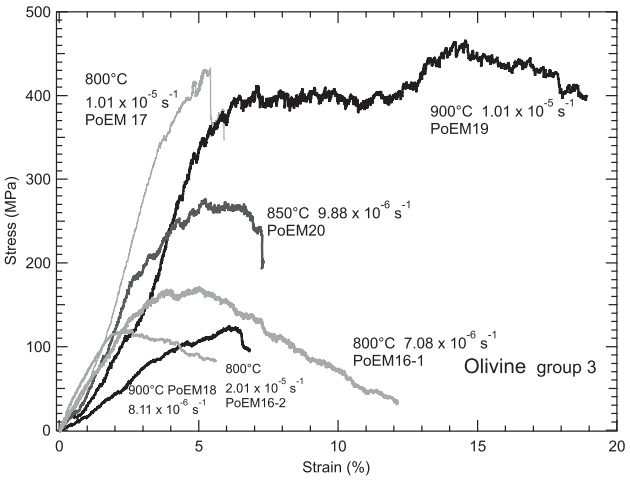

Fig. 5. Stress versus strain for constant displacement rate experiments for deformed olivine single crystals (group 3).

establishing the contact between the sample and the piston – the touch point) might be responsible for the observed abnormal low stress. The subsequent 'stick and slip' behavior during the rest of the experiment tends to corroborate this hypothesis. Interestingly, this experiment demonstrates that despite potential micro-cracking at the beginning of the deformation experiment, the sample can still hold stresses (>500 MPa) well above the confining pressure (300 MPa).

3.4. Orientations [0vw]

Tri-axial compression parallel to directions [0vw], that is between [001] and [010], permits to potentially activate one slip system: [001](010). The stress–strain curves for this group are shown in Fig. 4. Most runs show some work hardening, which in some cases becomes significant beyond a given strain only. This behavior is especially marked for PoEM 12 (900 °C, 1.02×10^{-5} s^{-1}) for which plastic flow occurred for about 5% under 300 MPa and is followed by strong work hardening leading to a maximum stress of 670 MPa. One experiment (PoEM 14) did not exhibit this behavior. It yielded under a low differential stresses (~150 MPa) and possibly even showed some softening. Stick–slip behavior was not clearly observed in this group, although the stress–strain curves are noisy for several experiments.

3.5. Orientations [uv0] and odd orientations

Compressive loading parallel to directions [uv0], that is between [100] and [010], favors [100] glide on (010). Odd orientations may activate a variety of slip systems. The stress–strain curves of olivine crystals from this group at various temperatures and constant displacement rates are shown in Fig. 5. The various experiments yield mechanical curves that are difficult to reconcile with a simple consistent influence of temperature or strain rate. The initial part of the curves (initial loading) exhibit very contrasted slopes which make yielding difficult to detect. The maximum stresses (400–450 MPa) were supported by two samples deformed at 800 and 900 °C at a strain rate of 1.01×10^{-5} s^{-1}. The experiment at the lowest temperature reached slightly higher stresses, but yielded at low strain. However, the samples with this orientation (group) reached some stress saturation, and exhibit instabilities. Other experiments exhibit strain softening after a maximum flow stress is reached. In one case (PoEM 18 deformation at 900 °C, 8.11×10^{-6} s^{-1}), loading, and potentially yielding as well, were very progressive. This experiment is one of those characterized by a very low maximum stress level (lower than the confining pressure). Stick–slip behavior was not observed for this group of orientations. Recovered samples exhibit asymmetric shapes (Fig. 1c) indicative of strong mechanical anisotropy and thus activation of a single slip system.

3.6. EBSD maps

We acquired EBSD orientation maps for the deformed samples PoEM 8, 9, 11, 15, 18, and 19. Selected orientation maps, misorientation profiles, and the corresponding pole figures are presented in Fig. 6. In the orientation maps, the red shade corresponds to the orientation defined as the initial one and the purple to blue shades permit quantifying the misorientation within the crystal. Significant misorientation (by lattice rotation) close to one end is visible in all studied samples and the profiles indicate up to 16° of rotation relative to the initial orientation in PoEM 18, where only one slip system should be, in theory, activated. The increase of misorientation as a function of distance is not as abrupt as expected in a well-developed sub-grain boundary. Finally, from the analysis of Fig. 6, it is evident that the fractures are post lattice rotation and hence post-deformation, since no misorientation gradient is associated with them.

3.7. TEM observations

All specimens investigated by TEM show pervasive evidence for dislocation activity and no evidence for brittle deformation (micro-cracking). In most cases, dislocations are in clear glide configurations and exhibit lattice friction. No subgrain boundaries have been found.

Among the specimens investigated (PoEM 8, 9, 11, 15, 18, and 19), only PoEM 8, which corresponds to the highest temperature tested in this study (1090 °C), exhibits a distinct microstructure. In this sample, which is oriented so as to activate several slip systems, namely [001](100), [100](001), [001](110), and [100](011), we do observe evidence of activation of both [100] and [001]-slip with comparable dislocation densities (compare Fig. 7a and b). [001] dislocations are wavy and exhibit very little preferred orientations (Fig. 7b). Numerous loops (either closed or open) are observed.

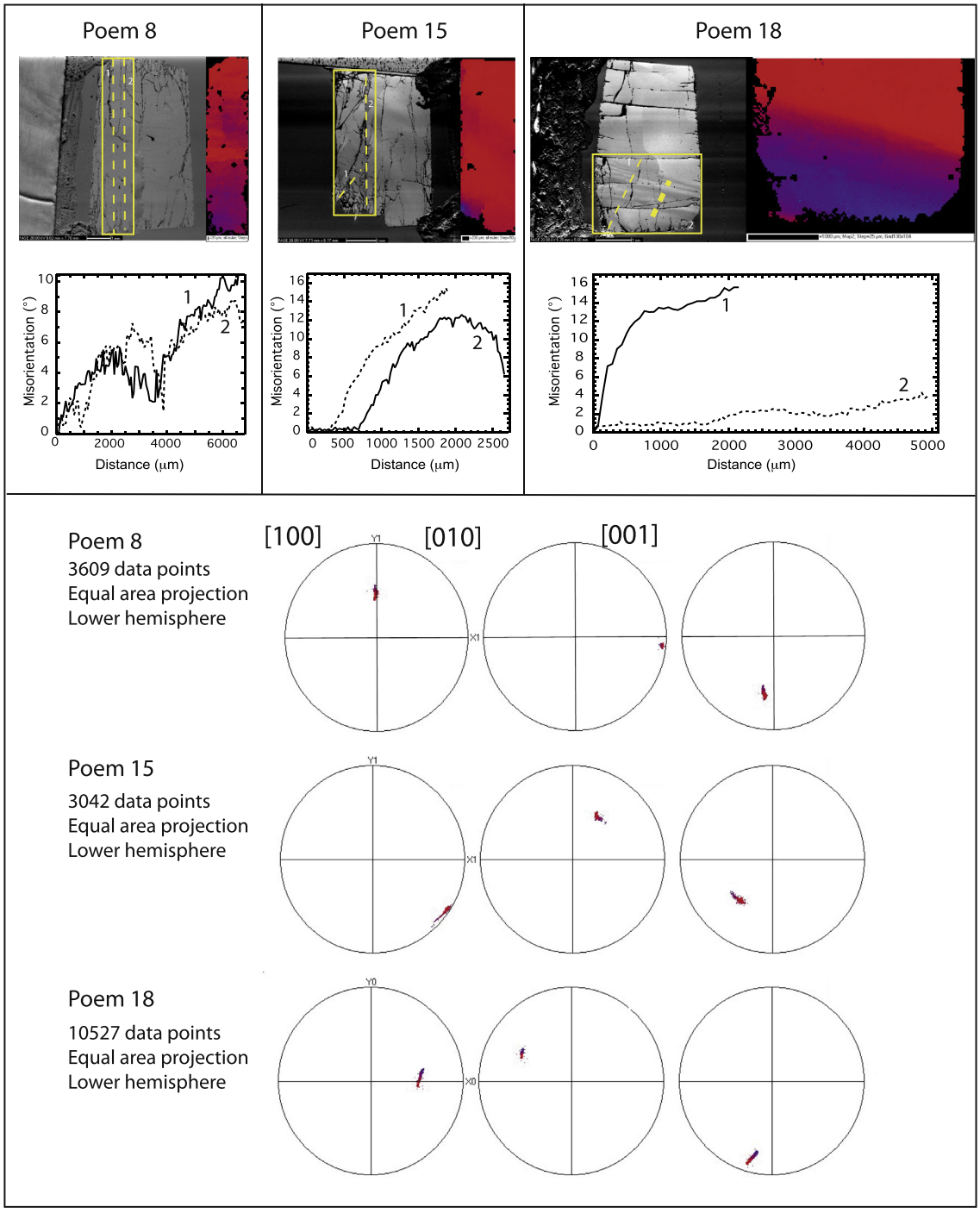

Fig. 6. SEM images, colored EBSD maps and misorientation profiles showing misorientation evolution along olivine single crystals, as well as corresponding pole figures for olivine section for PoEM 8, 15, and 18.

In all other specimens (PoEM 9, 11, 15, 18, and 19), the microstructure is dominated by [001] glide. [100] dislocations are very rarely observed, whatever the orientation of the compression. [001] dislocations exhibit long straight screw segments, which obviously face a high lattice friction (Fig. 7c and d). Observation of non-screw [001] dislocations is much less common. These non-screw segments are curved, showing that they bear no lattice friction. Non-screw dislocations gliding on adjacent planes often interact elastically leading to entanglements (Fig. 7d).

TEM observations have been made both within and outside the strongly misoriented zone (SMZ) of PoEM 15 (Figs. 6 and 7c and d). Outside the SMZ, the dislocation activity is low (probably the density is below 10^{10} m^{-2}, though TEM evaluations are not precise in this range of densities) and very heterogeneous. Indeed, at the TEM scale, large areas are free of dislocations. A few, rare [100] dislocations have been found. Within the SMZ, the dislocation microstructure is more homogeneous, being dominated by [001] dislocations with a density of $\sim$1–3 $\times$ 10^{13} m^{-2}. As already described, mobile non-screw segments glide and leave behind long straight screw dislocations (Fig. 7c). The fact that these screw dislocations can be observed in several instances shows that they belong to a glide plane which is not strongly inclined with respect to

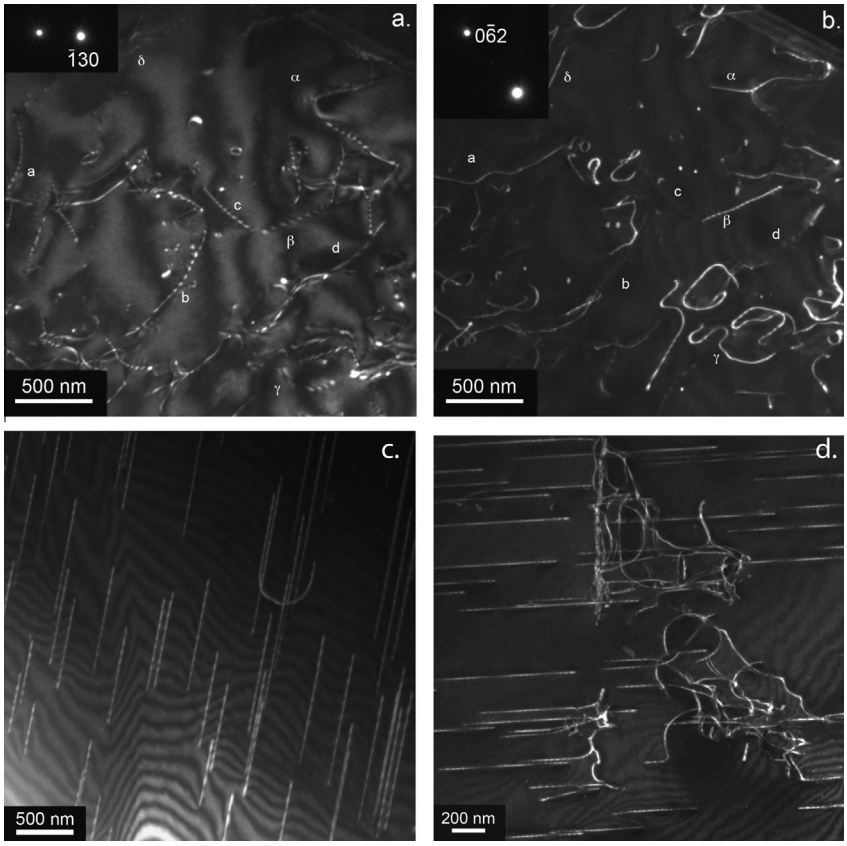

Fig. 7. Transmission electronic microscopy images: (a) PoEM8 (1090 °C). Weak-Beam Dark-Field (WBDF) micrographs close to the [3 1 3] zone axis showing two populations of dislocations. WBDF micrograph with g: $\bar{1}30$. [1 0 0] dislocations are in contrast (some labeled "a", "b", "c", and "d" are pointed). (b) WBDF micrograph of the same area with g: $0\bar{6}2$. [0 0 1] dislocations are in contrast ("α", "β", "γ", and "δ" are labeled on both micrograph). (c) PoEM15 (850 °C). Weak-Beam Dark-Field (WBDF) micrographs within the strongly misoriented zone (SMZ) with g: 2 2 2 close to the $[2\bar{1}\bar{1}]$ zone axis. [0 0 1] dislocations showing predominantly straight screw segments as well as one non-screw half loop. (d) PoEM 15 (850 °C). Weak-Beam Dark-Field (WBDF) micrograph with g: 0 0 4 close to the $[2\bar{1}0]$ zone axis showing dislocation entanglements.

the thin foil. The specimen shown on Fig. 7c has a mean orientation close to the $[2\bar{1}\bar{1}]$ zone axis. The $(1\bar{1}0)$ plane, which is inclined at *ca.* 24° is a good candidate to be the glide plane containing the observed screw dislocations.

4. Discussion

4.1. Plasticity and strain localization

Below 1000 °C, the present study reports dominance of [0 0 1] glide, whatever the direction of compression. Such predominance of [0 0 1] glide at low temperature was already reported by Raleigh (1968), but only two experiments were presented in that study. It was confirmed by subsequent studies in the 70s (e.g., Phakey et al., 1972). Above 1000 °C, the microstructures change drastically and both [1 0 0] and [0 0 1] glide are activated (PoEM 8, see Fig. 7). This change in behavior is consistent with data from experimental studies at higher temperature (*e.g.,* Durham and Goetze, 1977; Bai et al., 1991; Faul et al., 2011) and numerical modeling (Durinck, 2005; Durinck et al., 2007). Thus, the present studies suggest as well a change in olivine deformation from dominant [0 0 1] glide to equal activation of [1 0 0] and [0 0 1] glide above 1000 °C under experimental strain rates.

One should note, however, that despite the higher confining pressure used in the experiments of Phakey et al. (1972) or Raleigh (1968) (1 GPa and 0.5 GPa, respectively), it did not prevent strain localization and failures of some of their olivine crystals, as in this study. In most specimens, below 1000 °C, one observed significant strain localization associated with lattice rotation, which can provide further clue on the possible active slip plane.

4.2. Misorientations and lattice rotation

We have identified strong misorientation gradients within all olivine crystals investigated by EBSD mapping. In these zones, the lattice orientation rotates progressively; the cumulated misorientation ranges from 8° to 32°. At TEM scale there is no evidence of fracture, kink band, or sub-grain boundary formation (i.e., of a well-defined stepped change in crystallographic orientation accommodated by rows of organized dislocations at the nanoscale). Rather, these zones are characterized by a progressive increase in the dislocation density. For example, in PoEM 15, TEM observations have shown that the SMZ is associated with an increase of the density of [0 0 1] dislocations (Fig. 7c and d), probably gliding on {1 1 0} planes, which probably accommodated localized shearing of the crystal. Their analysis may thus provide further information on the active slip systems.

In previous low temperature studies (including Demouchy et al., 2009), the same phenomenon is likely to have occurred as well. Both Raleigh (1968) and Phakey et al. (1972) reported that undulatory extinction as well as possible kink bands (described as wavy slip bands by Raleigh, 1968) were present locally in many of their samples, but these observations and the related lattice misorientations could not be quantified by EBSD at that time.

To clearly visualize the local evolution of orientation (lattice rotation), the initial and final orientations of the compression axis as well as the 'activation fields' of all possible slip systems in oliv-

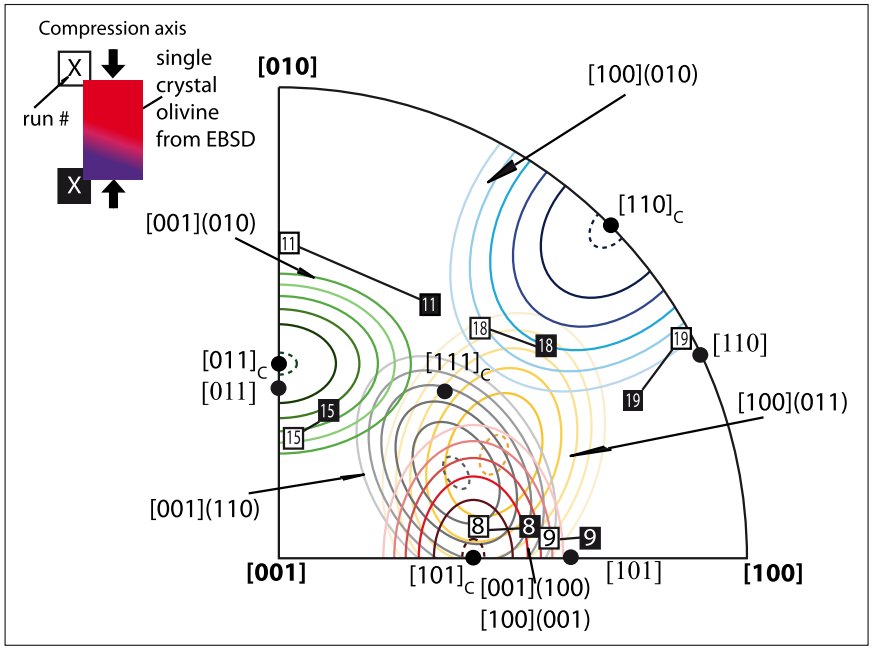

Fig. 8. Inverse pole figure of olivine showing the misorientation evolution. Slip systems with contours of Schmid's factor values for the different slip system expected to occurred in the plastic deformation of olivine are also shown: (010)[100], (011)[100], (010)[001], (110)[001], (100)[001], and (001)[100] (modified from Durinck, 2005). For clarity, Schmid's factor values ranges between 0.4 and 0.5. Additional direction are also shown: $[101]_c$ (45° from [100] and [001]), $[110]_c$ (45° from [100] and [010]), $[011]_c$ (45° from [001] and [010]) and $[111]_c$.

ine, defined as a function of their Schmid's factor contours as in Durinck (2005) and Farla et al. (2011), were plotted relative to the crystals orientation in an inverse pole figure (Fig. 8).

Plastic deformation by dislocation slip induces a lattice rotation with the following rotation vector:

$$r_1^s = \frac{1}{2}(m_{23}^s - m_{32}^s),\ r_2^s = \frac{1}{2}(m_{31}^s - m_{13}^s),\ r_3^s = \frac{1}{2}(m_{12}^s - m_{21}^s) \qquad (1)$$

where $m_{ij} = n_j b_i$ is the Schmid orientation tensor corresponding to the slip system with Burgers vector **b** and slip plane normal **n**. For the [001](110) slip system, this corresponds to a rotation vector parallel to $[1\bar{1}0]$. The lattice rotation associated with [001](110) is consistent with the rotation axes characterized by EBSD. For instance, PoEM 9 and 15 show [341] as an average rotation axis. Based on this convergence between EBSD misorientation data and TEM observation, we interpret the formation of these strong misorientation zones as the consequence of strain localization associated with [001](110) slip.

This instability of plastic deformation is likely to result from lack of degrees of freedom in the specimens deformation, since they may only activate 1 or 2 independent slip systems in each orientation (Fig. 8), and from the boundary conditions imposed by the strong alumina pistons (Fig. 1). The low dislocation mobility in the low temperature regime investigated here ($0.47\ T_m < T < 0.59\ T_m$), which is very far from the melting temperature (T_m = 1700 °C for Fo_{90}), is also very likely to lead to strain localization. These conditions may also account for the absence of steady state (with sometimes strain-hardening) observed in several runs. In spite of these limitations, the present results represent a substantial improvement of the existent data set and allow discussion of the rheology of olivine at low temperature.

4.3. Comparison with previous results at low temperature

The stresses as a function of temperature for all experiments, recalculated for a strain rate of $10^{-5}\ s^{-1}$, are reported in Fig. 9a and b. Stresses are plotted in Fig. 9a for 0.8–1% strain for a constant strain rate of $10^{-5}\ s^{-1}$ (i.e., before work-hardening starts) and the maximal stresses are plotted in Fig. 9b. Stresses for the [u0w] directions are in good agreement with the recent results by Demouchy et al. (2009) for single-crystals compressed along the $[101]_c$ direction. If the effect of pressure is taken into account, our results for [u0w] directions also agree with those from Durham and Goetze (1977), Phakey et al. (1972), and Raleigh (1968).

The measured stresses for other directions are, however, lower than the extrapolation of the results of Durham and Goetze (1977), which were obtained at significantly higher temperature (1150–1600 °C). They also do not agree with the low temperature results from Phakey et al. (1972), which are characterized by higher stresses. We attribute this discrepancy to work hardening with increasing strain observed in this study and in Phakey et al. (1972) and Raleigh (1968). Two other factors could explain differences in the mechanical data between the present and previous experiments. First, the sample size might come into question, since our samples are larger (cylinders with 4 × 6 mm in average) compared to the 1 × 1.5 × 1.5 parallelepipeds of Phakey et al. (1972) and thus deformation might have localized differently. Second, the chemical composition: our olivines are from mantle-derived peridotites from San Carlos (Arizona), while the olivines used in Phakey et al. (1972) were labeled as 'Red Sea', thus likely coming from the Zarbargad Island (Egypt), which is known for its large gem-quality hydrothermal olivines, which contain frequent clinohumite (hydrous) lamellae (Miller et al., 1987). Another and the most likely possibility is the overestimation of stresses in the previous experiments (which used a Griggs-type apparatus) due to several

factors such as the finite strength of the solid pressure medium and piston friction, which have been detailed by Tullis and Tullis (1986). Finally, the relatively low confining pressure in our study may have not allowed to achieve high enough stresses (>1 GPa) to affect the slip systems previously reported for olivine in aggregates, i.e., [100](010) or [001](010) at high temperature.

Recent experiments performed in D-DIA press have attempted to deform olivine at low temperature and high pressure (above 3 GPa) to avoid any risk of sample failure (Raterron et al., 2004; Mei et al., 2010; Long et al., 2011). In this type of experiment, the stresses increase as a function of decreasing temperature as for low-pressure experiments. Final differential stress obtained by Mei et al. (2010) are significantly higher than results from Griggs's apparatus experiments (Durham and Goetze, 1977; Phakey et al., 1972), which are in turn higher than results from this study and from Demouchy et al. (2009). Thus one can then question the relevance of a strong pressure effect (i.e., under a pressure too high for the uppermost mantle) and discard the results (Mei et al., 2010; Long et al., 2011). Nevertheless, when results from Long et al. (2011) are normalized to a strain rate of 10^{-5} s^{-1}, the differential stresses are in satisfying agreement with the hardness measurements of Evans and Goetze (1979). Finally, Raterron et al. (2004) experiments imply strengths significantly lower than all other existing data sets. As already discussed in the introduction, a possible explanation for the inconsistency between different DIA and D-DIA datasets (i.e., at high pressure) and with other data on olivine rheology at low temperature may be the lack of precision of the stress estimations in DIA and D-DIA experiments, since they can only be indirectly estimated from the broadening/refinement (i.e., for DIA set up) or shift (i.e., for D-DIA set up) of the X-ray diffraction peaks by the polycrystalline olivine itself or by external pistons.

4.4. New semi-empirical flow law and consequences for deformation of the uppermost mantle

To constrain the rheology of the lithospheric mantle, one needs to be able to extrapolate laboratory-based measurements to significantly slower strain rates. Most of the mechanical data compared above, even if obtained with different methods and showing evidence of composite behavior, agree with each other. One may thus

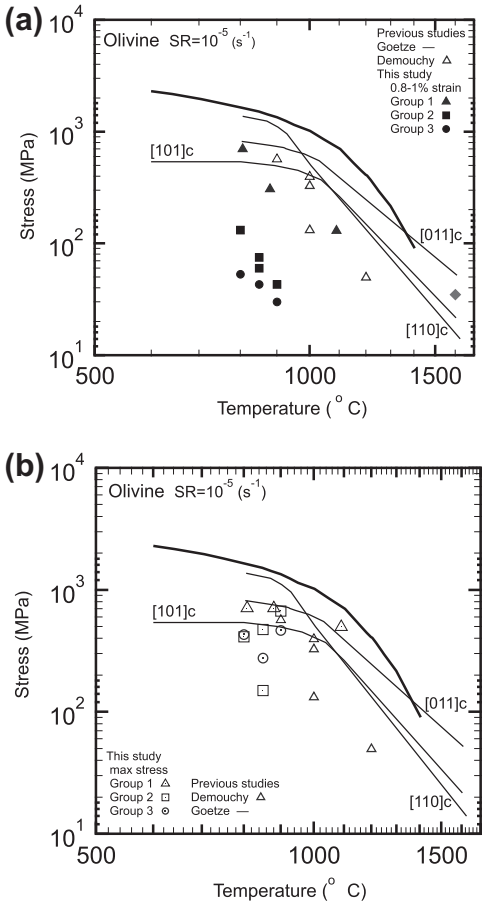

Fig. 9. Log–log diagram of differential stress (MPa) versus temperature (°C) for identical strain rate (10^{-5} s^{-1}) for the olivine crystals deformed in this study (a) for maximal stresses and (b) for a strain of 0.8%. For comparison, the results from Phakey et al. (1972) and Durham and Goetze (1977) and the change of the slip system as a function of temperature proposed by Goetze (1978) are also shown.

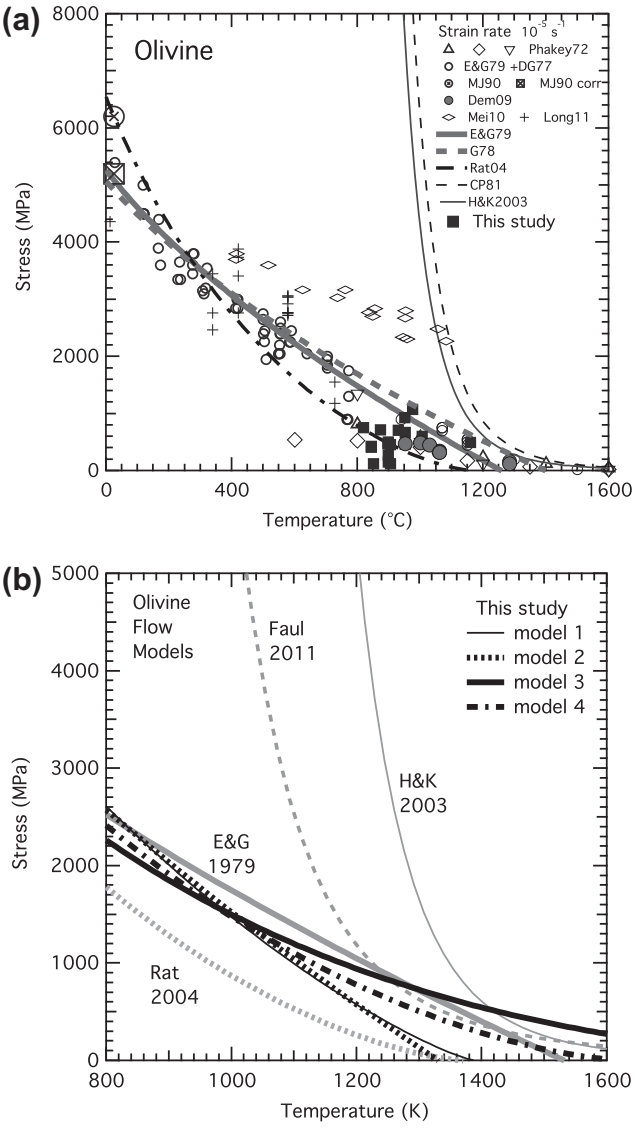

Fig. 10. Differential stresses (MPa) versus temperature (°C) (a) for all available mechanical data. All stresses were normalized to a strain rate of 10^{-5} s^{-1} (with Eq. (1)) except for a single datum point from Meade and Jeanloz (1990), see details in the main text. (b) Differential stresses (MPa) versus temperature (K). Fits to the data selection (for pressure ⩽3GPa and temperatures between 500 and 1000 °C, and a strain rate of 10^{-5} s^{-1}). The different models (best model is model 3) obtained in this study, as well as flow laws from *G78*: (1978), *E&G79*: Evans and Goetze (1979), *Rat04:* Raterron et al. (2004) and *H&K2003:* Hirth and Kohlstedt (2003), *Faul2011:* Faul et al. (2011) are also shown. Flow law parameters are reported in Table 2.

use them to define a semi-empirical flow law, which can be used to characterize the rheology of the uppermost mantle in numerical models of lithospheric deformation. For pressures and temperatures relevant of the uppermost mantle in continental and oceanic plates (pressures below 3 GPa and temperatures in the range 500–1000 °C), a meaningful data set of differential stresses is now available from experiments at strain rates of 10^{-5} s^{-1} as shown in Fig. 10a. Since the rheology of an aggregate will be controlled by the hardest slip system in the polycrystalline solid (Hull and Beacon, 1984), the highest stresses from single crystal data from Phakey et al. (1972), Demouchy et al. (2009), and from this study were selected. We have then added the indentation data from Evans and Goetze (1979), as well as the data from Durham and Goetze (1977) up to a temperature to 1100 °C to ensure a continuous transition to the high temperature dislocation creep regime (Hirth and Kohlstedt, 2003; Faul et al., 2011). Data from Long et al. (2011) for pressures ≈3 GPa were also added to the compilation. We did not add the single data point obtained by momentum-balanced from Meade and Jeanloz (1990) at high pressure because it was obtained at room temperature. However, if the shear stress from their experiment was converted to axial stress by assuming equivalent strain rate and not the identical nominal strain rate (i.e., axial stress = $\sqrt{3}$ × shear stress, as recommended by Paterson and Olgaard (2000)), this yields 5200 MPa at 0 °C, which is in agreement with the global distribution of the data for a temperature range from 25 to 1100 °C.

In this compilation, all temperatures were recalculated and normalized for an identical strain rate using the method proposed by Goetze (1978) as

$$T_{corr} = \left(\frac{1}{T_{exp}} + \frac{R\ln(\dot{\varepsilon}_{exp}/\dot{\varepsilon}_n)}{Q}\right)^{-1} \quad (2)$$

where T_{corr} is the corrected temperature for a given experiment, T_{exp} is the absolute temperature of the experiment, R is the gas constant, $\dot{\varepsilon}_{exp}$ and $\dot{\varepsilon}_n$ are the strain rate of the experiment and the strain rate desired for the normalization (here 10^{-5} s^{-1}), respectively. The activation energy Q is in J/mol, for which a first guess is made and then refined during the normalization prior to final fitting. Normalized data for all experiments are shown in Fig. 10a.

We can fit these data with the low temperature (T < 1200 °C) flow law provided by Evans and Goetze (1979) for iron-bearing olivine, where plastic flow of crystalline materials is expressed in terms of dislocation glide-controlled by lattice friction (Evans and Goetze, 1979; Frost and Ashby, 1982), with:

$$\dot{\varepsilon} = A\exp\left(-\frac{Q_p}{RT}\left[1-\left(\frac{\sigma}{\sigma_p}\right)^p\right]^q\right) \quad (3)$$

where T is the absolute temperature, A is a material parameter, σ_P is the Peierls stress and σ is the differential stress (both in GPa). The values of p and q are empirically determined and are generally bracketed by $0 \leqslant p \leqslant 1$ and $1 \leqslant q \leqslant 2$ (Frost and Ashby, 1982; Kocks et al., 1975, p. 142). Although they are essential and fundamental in the flow law, the p and q exponents are usually fixed prior to data fitting (Evans and Goetze, 1979; Raterron et al., 2004; Katayama and Karato, 2008; Mei et al., 2010; Faul et al., 2011). This strategy reduces the number of empirically determined parameters to only three instead of five parameters. However, this recurrent assumption recently led to contradictory low temperature flow laws (Table 2), since the p and q parameters strongly affect the curvature of the equation and the fitting of the data distribution (i.e., $q \approx 1$ is appropriate for a flat distribution as the one from Mei et al. (2010), and $q \approx 2$ for a curved distribution as from the current data compilation). Eq. (3) is more sensitive to p, q and σ_p than to A and Q, we have performed four types of fits (*i.e.,* least square fit of a user-defined function, with different initial values for every fitted parameter), leading to one preferred model. Data with and without normalization from Eq. (2) are not crucially different since Q is not the parameter controlling the curvature of the fit in Eq. (3). However, a second normalization was done using the output of the fitting to Eq. (3) and provided satisfying results. Values for parameters of each model are provided in Table 2 and the resulting flow laws are illustrated in Fig. 10b. Model 3, which best reproduces the selected data set for pressures below 3 GPa and temperature between 500 and 1000 °C, provides a very satisfying transition to the commonly used high temperature power flow law (*e.g.,* Hirth and Kohlstedt, 2003). The new semi-empirical flow law of an olivine rich aggregate is defined as

$$\dot{\varepsilon} = 1 \pm 0.2\times^6 \ \exp\left\{-\frac{450(\pm 60)\times 10^3}{RT}\left[1-\left(\frac{\sigma}{15\pm 4}\right)^{1/2}\right]^2\right\} \quad (4)$$

where T is the absolute temperature, R is the gas constant in J/Mol/K, and σ is the differential stress in GPa. At temperatures relevant of the lithospheric mantle, model 3 leads to stresses significantly lower than those predicted by the flow laws of Goetze (1978) and Evans and Goetze (1979), but stresses higher than those predicted by the flow law from Raterron et al. (2004). At first, the differences between the three flow laws are not striking, but we have now more precise values for temperatures relevant of the uppermost mantle

Table 2
Compilation of published semi-empirical low temperature flow laws for olivine and best-fitted results to data compilation from this study.

Reference	T (°C)	Strain rate (s^{-1})	Pressure (GPa)	A (s^{-1})	Q (kJ/mol)	σ_p (GPa)	p	q	Notes
Goetze (1978)[1]	27–1500	10^{-7}–10^{-5}	n.d.[1]	5.7×10^{11}	535	8.5	1	2	Data compilation
Evans and Goetze (1979)[2]	27–1500	10^{-7}– 10^{-5}	n.d.[2]	1.3×10^{12}	502	9.1	1	2	Hardness measurements
Raterron et al. (2004)[3]	400–890	n.d.[3]	4.9–9.20	2.6×10^{16}	564	15.4	2/3	2	Dia experiments- relaxation
Mei et al. (2010)[4]	400–1000	0.1–6.81 × 10^{-5}	4.5–9.45	1.4×10^{-7}	320	5.9	1/2	1	D-Dia experiments
Long et al. (2011)	25–400	10^{-7} –10^{-5}	3–5	6.75×10^{9}	458	6.7	3/4	4/3	D-Dia experiments Lattice friction controlled creep
Long et al. (2011)	400–1000	10^{-7} –10^{-5}	3–5	1×10^{6}	1480	2.8	1	1	D-Dia experiments Discrete obstacles controlled creep
Model 1 – This study	500–1100	10^{-7} –10^{-4}	⩽3	4.9×10^{7}	338	15.0	4/5	2	This study + selected published data
Model 2 – This study	500–1100	10^{-7} –10^{-4}	⩽3	1.0×10^{8}	331	11.4	1	2	This study + selected published data
Model 3 – This study	500–1100	10^{-7} –10^{-4}	⩽3	1.0×10^{6}	450	15.0	1/2	2	This study + selected published data
Model 4 – This study	500–1000	10^{-7} –10^{-4}	⩽3	2.4×10^{7}	386	15.1	2/3	2	This study + selected published data

Nota 1: Vicker indentation experiments (hardness measurements, see Evans and Goetze, 1979) performed at room pressure, but during deformation the olivine slab locally experienced a confining pressure equivalent to 2 GPa (D.L. Kohlstedt, perso. comm.). Other experiments were performed using an 1- atm creep apparatus (Durham and Goetze, 1977) and in a Grigg's apparatus (Phakey et al., 1972).
Nota 2: Article presenting the data used in the compilation by Goetze (1978), even if the latter article got published first.
Nota 3: Strain rates are not listed in the original publication but are estimated to be around 10^{-5} s^{-1}.
Nota 4: The A material constant is in s^{-1} MPa^{-2} since a term σ^2 was added in front of the exponential term, see Frost and Ashby (1982), Mei et al. (2010).
Abbreviation: D-Dia, deformation-DIA press (Wang et al., 2003).

(800–1100 °C). In addition, the previous flow laws did not crosscut the usual high-temperature power flow laws, their use results therefore in a discontinuity in the description of the olivine mechanical behavior with increasing temperature, even at laboratory strain rates. This problem is not present when using Eq. (4) to describe the low temperature deformation (Fig. 10).

Deformation experiments in laboratory are always performed at strain rates extremely fast compare to strain rates induced by mantle convection and associated to plate tectonic dynamics. Thus it is necessary to extrapolate experimental results to very slow strain rates to discuss their consequences for the mantle dynamics. The new flow law proposed here is compared to previous low and high temperature flaw laws in Fig. 11, where each flow law is shown for two strain rates: $1 \times 10^{-5}\,s^{-1}$ (*i.e.,* corresponding to strain rates easily achievable in laboratories) and $1 \times 10^{-14}\,s^{-1}$ (i.e., corresponding to strain rate relevant of the mantle lithosphere). The flow law proposed in this study ensures a smooth transition to the high temperature flow law defined in Hirth and Kohlstedt (2003) even at geological strain rates.

The present results imply that the strength of lithospheric mantle has been significantly overestimated and that the transition to low temperature plasticity (*i.e.,* power law breakdown) may occur at higher temperatures than predicted using previous flow laws, such as the one proposed by Evans and Goetze (1979). Another consequence of this new flow law is that the presence of small amount of melt or incorporation of hydrogen in olivine (even at the ppm level) may not be required to reconcile the observations indicating a weak strength of Earth's uppermost mantle lithosphere and the experimentally obtained rheology of olivine.

5. Conclusions

Deformation experiments in tri-axial compression on olivine single crystals were performed at temperatures relevant to the uppermost lithospheric mantle and at a confining pressure of 300 MPa. The main results of this experimental study are the following: (i) a dependence of the glide mechanism in olivine on temperature is confirmed, with predominance of [001] glide below 1000 °C at laboratory strain rates. (ii) EBSD and TEM analyses demonstrated that deformation localization occurs in olivine single crystals, yielding composite mechanical behavior, probably associated with the slow mobility of dislocations at low temperature and the strong plastic anisotropy of olivine (see Tommasi et al., 2009). (iii) The strength of olivine crystals at temperatures prevailing in the lithospheric mantle is significantly lower than inferred from extrapolation of high-temperature flow laws. Based on these data, we propose a new flow law for olivine at temperatures appropriate for the uppermost mantle. This flow law suggests that the occurrence of low fractions of melt or incorporation of hydrogen in the olivine atomic structure are not required to reconcile the observed low strength of Earth's uppermost mantle and the experimentally obtained flow laws. It also predicts a consistent transition to high temperature flow laws at >1100 °C for strain rates relevant for the lithospheric mantle.

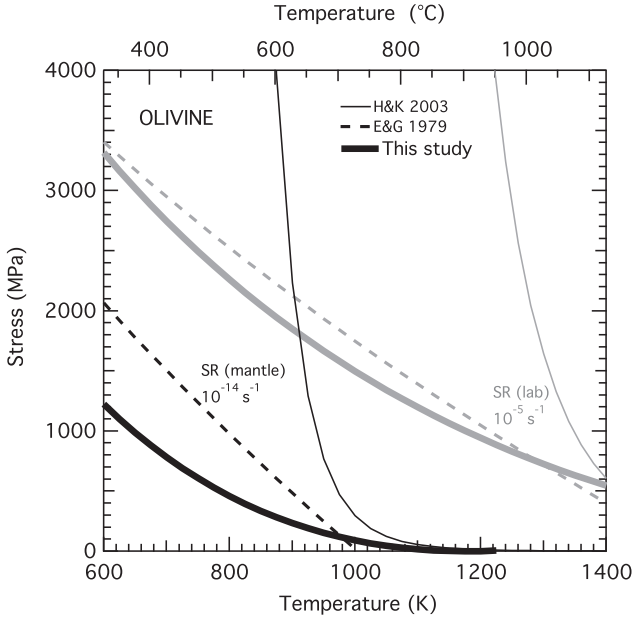

Fig. 11. Differential stress as a function of temperature for both laboratory and geological strain rates (SR) determined using the flow laws from *E&G79*: Evans and Goetze (1979), *H&K2003*, Hirth and Kohlstedt (2003) and the one obtained in this study (model 3).

Acknowledgments

A Marie Curie fellowship awarded to S.D. (PoEM: Plasticity of Earth Mantle, FP7-PEOPLE-20074-3-IRG, N°230748-PoEM) supported this study. S.D. is grateful to Prof. D.L. Kohlstedt, Dr. M.E. Zimmerman, Dr. D. Mainprice and Dr. A. Vauchez for profitable discussions at an early stage of this research. Prof I. Jackson is thanked for his helpful review. Prof. H. Keppler is thanked for access to the X-ray diffraction lab of the Bayerisches Geoinsitut (Univ. Bayreuth, Germany). C. Nevado and D. Delmas are thanked for providing high-quality thin sections for SEM and TEM. F. Barou is thanked for help with SEM-EBSD analyses. J. Oustry is sincerely thanked for his help and support in the mechanical workshop. FTIR analyses were performed with the support of D. Maurin at the Lab. Colloids, Verre et Nanomateriaux at Université de Montpellier 2. The TEM and EBSD-SEM national facilities in Lille and Montpellier are supported by the Institut National de Sciences de l'Univers (INSU) du Centre National de la Recherche Scientifique (CNRS, France). The EBSD-SEM facility in Montpellier and TEM facility in Lille are also supported by the Conseil Régional Languedoc-Roussillon (France) and by the Conseil Régional du Nord-Pas de Calais, (France), respectively.

References

Bai, Q., Kohlstedt, D.L., 1992. High-temperature creep of olivine single crystals III. Mechanical results for unbuffered samples and creep mechanisms.. Philos. Magn. A 66 (6), 1149–1181.

Bai, Q., Mackwell, S., Kohlstedt, D., 1991. High-temperature creep of olivine single crystals. 1. Mechanical results for buffered samples.. J. Geophys. Res. 96 (B2), 2441–2463.

Bell, D., Rossman, G., Maldener, J., Endisch, D., Rauch, F., 2003. Hydroxide in olivine: a quantitative determination of the absolute amount and calibration of the IR spectrum. J. Geophys. Res. 108 (B2).

Berry, A., O'neill, H.S., Hermann, J., Scott, D.R., 2007. The infrared signature of water associated with trivalent cations in olivine. Earth Planet. Sci. Lett. 261, 134–142.

Bolfan-Casanova, N., Keppler, H., Rubie, D., 2000. Water partitioning between nominally anhydrous minerals in the $MgO–SiO_2–H_2O$ system up to 24 GPa: implications for the distribution of water in the Earth's mantle. Earth Planet. Sci. Lett. 182, 209–221.

Chen, S., Hiraga, T., Kohlstedt, D.L., 2006. Water weakening of clinopyroxene in the dislocation creep regime. J. Geophys. Res.. http://dx.doi.org/10.1029/2005JB003885.

Chopra, P.N., Paterson, M.S., 1984. The role of water in the deformation of dunite. J. Geophys. Res. 89, 7861–7876.

Demouchy, S., Schneider, S.E., Mackwell, S.J., Zimmerman, M.E., Kohlstedt, D.L., 2009. Experimental deformation of olivine single crystal at lithospheric temperature. Geophys. Res. Lett. 36, L04304.

Demouchy, S., 2010. Diffusion of hydrogen in olivine grain boundaries and implications for the survival of water-rich zones in the Earth's mantle. Earth Planet. Sci. Lett. 295, 305–313.

Demouchy, S., Tommasi, A., Barou, F., Mainprice, D., Cordier, P., 2012. Deformation of olivine in torsion under hydrous conditions. Phys. Earth Planet. Inter. 202–203, 57–70.

Deer, W.A., Howie, R.A., Zussman, J., 1997. Rock-Forming Minerals Orthosilicates. The Geological Society, 919 pp..
Durham, W.B., Ricoult, D.L., Kohlstedt, D.L., 1985. Interaction of slip systems in olivine. In: Schock, R.N. (Ed.), Point Defects in Minerals, Geophys. Monogr. Ser., vol. 31. AGU, Washington, DC, pp. 185–193.
Durham, W.B., Goetze, C., 1977. Plastic flow of oriented single crytals of olivine: 1 – mechanical data. J. Geophys. Res. 82 (36), 5737–5753.
Durinck, J., 2005. Approche numérique de la plasticité de la forsterite aux échelles atomique et microscopique. Ph.D. thesis. University des Sciences et Technologies de Lille, UFR de Physique, France, pp 197.
Durinck, J., Devincre, B., Kubin, L.P., Cordier, P., 2007. Modeling the plastic deformation of olivine by dislocation dynamics simulations. Am. Mineral. 92, 1346–1357.
Evans, B., Goetze, C., 1979. The temperature variation of hardness of olivine and its implication for polycrystalline yield stress. J. Geophys. Res. 84, 5505–5524.
Farla, R.J.M. et al., 2011. Slip-system and EBSD analysis on compressively deformed fine-grained polycrystalline olivine. In: Prior, D.J., Rutter, E.H., Tatham, D.J.e. (Eds.), Deformation mechanism, Rheology and Tectonics: Microstructures, Mechanics and Anisotropy. Special Publications, Geological Society, London.
Faul, U.H., Gerald, J.F., Farla, R.J.M., Ahlefeldt, R., Jackson, I., 2011. Dislocation creep of fine-grained olivine. J. Geophys. Res 116. http://dx.doi.org/10.0129/2009JB007174.
Frost, H.J., Ashby, M.F., 1982. Deformation mechanism maps: the plasticity and creep of metals and ceramics. Pergamon press, Oxford, 166 pp..
Gaboriaud, R.J., Darot, M., Gueguen, Y., Woirgard, J., 1981. Dislocations In olivine indented at low-temperatures, Phys. Chem. Miner. 7 (2), 100–104.
Girard, J., Chen, J., Raterron, P., Holyoke, C., 2010. Deformation of single crystal sample using D-DIA apparatus coupled with synchrotron X-rays: in situ stress and strain measurements at high pressure and temperature. J. Phys. Chem. Solids 71, 1053–1058.
Goetze, C., 1978. The mechanism of creep in olivine. Philos. Trans. R. Soc. Lond. A 288, 99–119.
Griggs, D.T., 1967. 1967, Hydrolytic weakening of quartz and other silicates. Geophys. J. R. Astron. Soc. 14, 19–31.
Hirth, G., Kohlstedt, D.L., 1996. Water in the oceanic upper mantle: implications for rheology, melt extraction and the evolution of the lithosphere. Earth Planet. Sci. Lett. 144, 93–108.
Hirth, G., Kohlstedt, D.L., 2003. Rheology of the upper mantle and the mantle wedge: a view from the experimentalists. In: Eiler, J. (Ed.), Inside the Subduction Factory. American Geophysical Union, Washington, DC, pp. 83–105.
Hull, D., Bacon, D.J., 1984. Introduction to dislocation. International Series on Materials Science and Technology, vol. 37. Pergamon Press, New York.
Jacobsen, S.D., Demouchy, S., Frost, D.J., Boffa-Ballaran, T., 2005. A systematic study of OH in hydrous wadsleyite from polarized infrared spectroscopy and single-crystal X-ray diffraction: oxygen sites for hydrogen storage in Earth's interior. Am. Mineral. 90, 61–70.
Karato, S.I., Paterson, M.S., Fitzgerald, J.D., 1986. Rheology of synthetic olivine aggregates: influence of grain size and water. J. Geophys. Res. 91, 8151–8176.
Katayama, I., Karato, S., 2008. Low-temperature, high-stress deformation of olivine under water-saturated conditions. Phys. Earth Planet. Inter. 168, 125–133.
Kocks, U.F., Argon, A.S., Ashby, M.F., 1975. Thermal activation. In: Kocks, U.F., Argon, A.S., Ashby, M.F. (Eds.), Thermodynamics and Kinetics of Slip. Pergamon Press, pp. 110–271.
Kohlstedt, D.L., Goetze, C., 1974. Low-stress high-temperature creep in olivine single crystals. J. Geophys. Res. 79, 2045–2051.
Libowitzky, E., Rossman, G.R., 1997. An IR absorption calibration for water in minerals. Am. Mineral. 82, 1111–1115.
Long, H., Weidner, D.J., Li, L., Chen, J., Wang, L., 2011. Deformation of olivine at subduction zone conditions determined from in situ measurements with synchrotron radiation. Earth Planet. Sci. Lett. 186, 23–35.
Meade, C., Jeanloz, R., 1990. The strength of mantle silicates at high pressures and room temperature: implications for the viscosity of the mantle. Nature 348, 533–535.
Mei, S., Kohlstedt, D.L., 2000a. Influence of water on the plastic deformation of olivine aggregates: 1. Diffusion creep regime. J. Geophys. Res. 105 (21), 21457–21469.
Mei, S., Kohlstedt, D.L., 2000b. Influence of water on plastic deformation of olivine aggregates 2. Dislocation creep regime. J. Geophys. Res. 105 (9), 21471–21481.
Mei, S., Suzuki, A., Kohlstedt, D.L., Dixon, N.A., Durham, W.B., 2010. Experimental constraints on the strength of the lithospheric mantle. J. Geophys. Res. 115. http://dx.doi.org/10.1029/2009/JB006873.
Miller, G.H., Rossman, G.R., Harlow, G.E., 1987. The natural occurence of hydroxide in olivine. Phys. Chem. Minerals 14, 461–472.
Morniroli, J.P., Steeds, J.W., 1982. Microdiffraction as a toll for crystal-structure identification and determination. Ultramicroscopy 45, 219–239.
Mosenfelder, J.L., Sharp, T.G., Asimow, P.D., Rossman, G.R., 2006. Hydrogen incorporation in natural olivine. In: Jacobsen, S.D.v.d.L.S. (Ed.), Earth's Deep Water Cycle. AGU, Washington, DC, pp. 45–56.
Paterson, M., 1982. The determination of hydroxyl by infrared absorption in quartz, silicate glasses and similar materials. Bull. Mineral. 105, 20–29.
Paterson, M.S., Olgaard, D.L., 2000. Rock deformation tests to large shear strains in torsion. J. Struct. Geol. 22, 1341–1358.
Phakey, P., Dollinger, G., Christie, J., 1972. Transmission electron microscopy of experimentally deformed olivine crystals. In: Heard, H.C., Borg, I.Y., Carter, N.L. (Eds.), Flow and Fracture of Rocks. Am. Geophys. Un. Geophys. Monogr. Series.
Raleigh, C.B., 1968. Mechanism of plastic deformation of olivine. J. Geophys. Res. 73, 5391–5406.
Raterron, P., Girard, J., Chen, J., 2012. Activities of olivine slip systems in the upper mantle. Phys. Earth Planet. Inter. 2012, 105–112.
Raterron, P., Wu, Y., Weidner, D.J., Chen, J., 2004. Low-temperature olivine rheology at high pressure. Phys. Earth Planet. Inter. 145, 149–159.
Tommasi, A., Knoll, M., Vauchez, A., Signorelli, J., Thoraval, C., Logé, R., 2009. Structural reactivation in plate tectonics controlled by olivine crystal anisotropy. Nat. Geosci. 2, 423–427. http://dx.doi.org/10.1038/NGEO528.
Tullis, T., Tullis, J., 1986. Experimental rock deformation techniques. In: Hobbs, Heard (Ed.), Mineral & Rock Deformation: Laboratory Studies, vol. 36, pp. 297–324.
Wang, Y., Durham, W., Getting, I., Weidner, D., 2003. The deformation-DIA: a new apparatus for high temperature triaxial deformation to pressure up to 15 GPa, Rev. Sci. Instru. 74 (6), 3002–3011.
Withers, A.C., Bureau, H., Raepsaet, C., Hirschmann, M.M., 2012. Calibration of infrared spectroscopy by elastic recoil detection analysis of H in synthetic olivine. Chem. Geol. 334, 92–98.